Adsorption of CO_2 on Amorphous and Crystalline Zirconia: A DFT and Experimental Study

Tatsuya Joutsuka[a,b] and Shohei Tada*[c]*

[a] *Department of Materials Science and Engineering, Ibaraki University, 4–12–1 Nakanarusawa-cho, Hitachi, Ibaraki 316–8511, Japan.*

[b] *Frontier Research Center for Applied Atomic Sciences, Ibaraki University, 162–1 Shirakata, Tokai, Ibaraki 319–1106, Japan.*

[c] *Department of Applied Science and Engineering, School of Engineering, Hokkaido University, Kita 13, Nishi 8, Kita-ku, Sapporo, Hokkaido 060-8628, Japan.*

AUTHOR INFORMATION

Corresponding Author

* E-mail: T.J.: tatsuya.joutsuka.joe@vc.ibaraki.ac.jp; S.T.: shohei.tada.st@eng.hokudai.ac.jp

ABSTRACT

Herein, we study the structural and electronic origins of molecular adsorption using experiments and density functional theory (DFT) calculations. We performed X-ray diffraction (XRD) and temperature-programmed desorption (TPD) of CO_2 on amorphous zirconia (*am*-ZrO_2) and crystalline (tetragonal and monoclinic) zirconia. Using molecular dynamics simulations, the bulk structures of *am*-ZrO_2 and *am*-zirconium(IV) hydroxide (*am*-$Zr(OH)_4$) were obtained and the reproducibility of the experimental structure was confirmed by comparing the radial distribution functions. In addition, the hydroxyl density on the hydrogenated ZrO_2 surfaces was found to be consistent with the experimental results. Both experiments and simulations indicate that the adsorption of CO_2 on an *am*-ZrO_2 surface is more heterogeneous and weaker than that on a crystalline zirconia surface. Because the charge environment and band structures of crystalline zirconia are approximately the same as those of *am*-ZrO_2, the weak adsorption on the *am*-ZrO_2 surface arises from the fewer and stronger Zr-O bonds on the surface. These findings provide molecular-level insight not only for the adsorption of CO_2 but also into the molecular adsorption on ZrO_2-based catalysts.

KEYWORDS Zirconia, DFT calculation, Amorphous, Adsorption

1 Introduction

Zirconium oxides, ZrO_2, and zirconium hydroxides, $Zr(OH)_4$, also called hydrous zirconia, are important materials for various scientific and industrial applications, such as catalysts[1, 2] and adsorbents.[3, 4] One of the most important applications is methanol synthesis by CO_2 hydrogenation for the reuse of CO_2 to reduce greenhouse gas emissions. To control the absorption and reactivity of CO_2, morphology dependence is crucial,[1, 5, 6] and experimental preparations can control the morphology of zirconia. For example, the dehydration of amorphous (*am*)-$Zr(OH)_4$ results in amorphous zirconia (*am*-ZrO_2). Starting from *am*-$Zr(OH)_4$, calcination vaporizes internal water to yield *am*-ZrO_2 at intermediate temperatures, which in turn changes to tetragonal (*t*)-ZrO_2 and monoclinic (*m*)-ZrO_2 at higher temperatures.[2, 7, 8] $Zr(OH)_4$ is also employed to adsorb hazardous chemicals, such as toxic industrial compounds and chemical warfare agents,[4] because $Zr(OH)_4$ forms a high-surface-area powder with a high density of chemically active hydroxyl (OH) groups.

Despite the significance of amorphous zirconia, the molecular-level understanding of the relationship between morphology-dependent adsorption capacity and surface structure remains both experimentally and theoretically elusive. The difficulty between the experimental and theoretical analyses is mainly due to the heterogeneity of the amorphous structure. Although molecular dynamics (MD) simulations can elucidate the microscopic structure and mechanism of the catalytic reactions, it remains computationally challenging to model the heterogeneous surfaces of *am*-$Zr(OH)_4$ and *am*-ZrO_2. Some experimental studies have reported morphology-dependent adsorption capacity,[9] but the relationship with the surface structure at the atomic level remains unclear.

Here, we elucidate the bulk and surface structures of *am*-$Zr(OH)_4$, *am*-ZrO_2, *t*-ZrO_2, and *m*-ZrO_2 using experimental and density functional theory (DFT) calculations, with a focus on the structural effects of zirconia on molecular absorption. X-ray diffraction (XRD) and temperature-programmed desorption (TPD) of CO_2 were performed for amorphous and crystalline zirconia to understand the adsorption behavior of CO_2. For the calculations, *am*-ZrO_2 was prepared by melting and subsequent cooling (annealing) using *ab initio* MD (AIMD) simulations. A comparison of the radial distribution functions (RDFs) of *am*-$Zr(OH)_4$ and *am*-ZrO_2 with the experimental results confirmed that the amorphous structure was reproduced by our MD simulations. The adsorption energy of CO_2 was compared among all the phases of zirconia to understand the adsorption of CO_2 molecules. Furthermore, we analyzed the surface structure and computed the density of states to elucidate the origin of the characteristic adsorption on the amorphous zirconia surfaces.

The remainder of this paper is organized as follows. In Section 2, the experimental and computational conditions are described. Experimental (XRD and CO_2-TPD) and computational (bulk and surface structures of zirconia and adsorption energies) results are discussed in Sections 3 and 4 to elucidate the morphology-dependent adsorption capacity. Finally, section 5 summarizes the study.

2 Methods

2.1 Experimental Conditions

2.1.1 Catalyst preparation

We used two types of zirconia as received: *am*-ZrO_2 (Daiichi Kigenso Kagaku Kogyo, NND) and *m*-ZrO_2 (NIPPON DENKO, PCS90). The former was named Zr-1, and the latter was named Zr-3. We prepared Zn-doped ZrO_2 as *t*-ZrO_2 according to our previous work.[10] First, *am*-ZrO_2 was impregnated with an aqueous solution of Zn nitrate (Fujifilm Wako), and then dried at 110 °C. Next, the obtained powder was calcined at 500 °C for 3 h. The Zn/(Zn+Zr) atomic ratio was 7%. The Zn-doped ZrO_2 was named Zr-2.

2.1.2 Characterization

The crystal structure was determined using an X-ray diffractometer (Rigaku, Ultima IV). The sample powder was mounted on a glass plate and the plate was placed in the diffractometer. The X-ray source was CuKα (λ = 0.15406 nm) with an accelerating voltage of 40 kV and a tube current of 40 mA. The scanning rate was 10° min^{-1}.

N_2 adsorption at liquid nitrogen temperature (-196 °C) was performed using an automatic volumetric adsorption apparatus (Microtrac BEL, BELSORP mini-II, and BELPREP vac-II). Before the measurement, 150 mg sample was put in a sample tube and dried under vacuum at 300 °C for 3 h. The specific surface area and pore volume were calculated based on the Brunauer–Emmett–Teller (BET) theory.

CO_2 adsorption was measured using temperature-programmed desorption (TPD). In an N_2 flow, 200 mg of the sample was heated at 300 °C for 3 h (MicrotracBEL, BELCAT II). Subsequently, the sample was cooled down to 50 °C and contacted with 10% CO_2/N_2 at a flow rate of 50 mL min^{-1}. Finally, the sample was heated to 800 °C at a ramping rate of 5 °C min^{-1} under an N_2 flow (50 mL min^{-1}). The CO_2 composition of the outlet gas was measured using a

CO_2 meter (VAISALA, GM70J0A1C0A0J). Peak separation was performed using the XPSPEAK 4.1.

2.2 Computational Conditions

We performed DFT calculations with the Perdew-Burke-Ernzerhof (PBE)[11] exchange and correlation functional and D3 correction[12] using cp2k program package.[13] The Goedecker-Teter-Hutter pseudopotentials[14, 15] and a double-ζ valence plus polarization (DZVP-MOLOPT-SR-GTH[16]) Gaussian basis set for the orbitals were used. The cutoff associated with mapping Gaussians onto a multi-grid was 60 Ry and the planewave cutoff for the finest level of the multi-grid was 400 Ry. Only the Γ point was employed for *k*-point sampling using large supercells, as explained below. The target accuracy for the SCF convergence was 10^{-5}.

To examine the stability of zirconia surfaces, we calculated the surface energy defined by

$$\gamma = \frac{E_{\text{surf}} - N_{\text{surf}} E_{\text{bulk}}}{2S}, \tag{1}$$

where N_{surf} is the number of ZrO_2 units in the slab, S is the surface area of the supercell, and E_{surf} is the total slab energy. E_{bulk} is the energy per formula unit of the bulk phase.

In addition, to investigate the stability of adsorbed CO_2, the adsorption energy was computed as

$$E_{\text{ads}} = E(\text{substrate+adsorbate}) - E(\text{substrate}) - E(\text{adsorbate}), \tag{2}$$

where E(substrate − adsorbate), E(substrate), and E(adsorbate) are the energies of the adsorbed complex, substrate, and adsorbate, respectively. According to this definition, a lower adsorption

energy indicates stable adsorption. It should be noted that in the case of adsorption at the *am*-$Zr(OH)_4$ and *am*-ZrO_2 surfaces, each adsorbate was adsorbed on at least 10 Zr sites at the surface, and this study reports mainly the minimum adsorption energy that is the most relevant to the experiment. However, larger adsorption energies exist owing to the surface heterogeneity, and the distribution is discussed in **Section 3.5.2** at *am*-ZrO_2. In addition, Section S2 also reports the adsorption energies of H_2, H_2O, and CH_3OH (the reactant and product in CO_2 hydrogenation to methanol) and shows that molecular adsorption on *am*-ZrO_2 surface is weaker than that on crystalline zirconia surfaces.

2.2.1 *am*-$Zr(OH)_4$

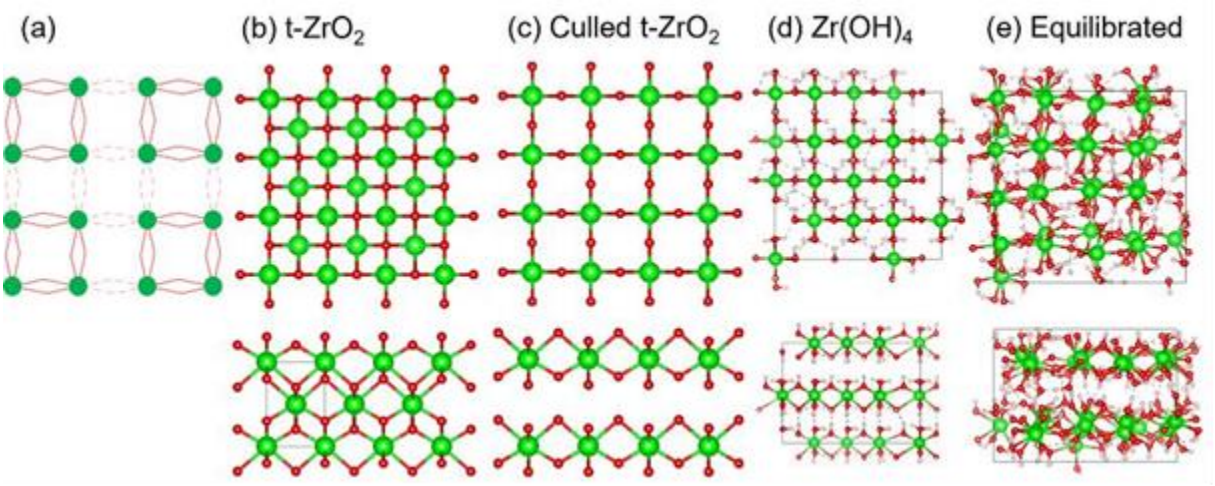

Figure 1. (a) Schematic illustration of cyclic tetramer of $Zr(OH)_4$. Green circles, solid lines, and dashed lines respectively represent the Zr atoms, hydroxyl bridges inside and outside the tetramers. Top and side views of (b) *t*-ZrO_2, (c) culled *t*-ZrO_2, (d) initial and (e) equilibrated configurations of $[Zr(OH)_4]_{32}$. The black lines in (b) are the boundaries of the unit cell of *t*-ZrO_2, while those in (d) and (e) delimit the supercells. The dashed lines in (d) and (e) represent hydrogen bonds. Color code: green, Zr; red, O; white, H. The figures are drawn by VESTA.[17]

The structure of bulk *am*-$Zr(OH)_4$ assumes a (square-planar) cyclic tetramer of $Zr(OH)_4$ units, as illustrated in **Figure 1a**.[4, 18, 19] In the tetramer, Zr atoms are connected by OH groups, and each tetramer forms a hydrogen-bond network. To prepare such a structure, we culled the central ZrO_2 layer in the *t*-ZrO_2 crystal structure[20] (**Figure 1b**) for the initial configuration of $Zr(OH)_4$ (**Figure 1c**) because the tetramer has a framework similar to that of the Zr–O bonds, as illustrated in **Figure 1a**. Attaching H atoms to O atoms in the culled structure results in a supercell of 32 $Zr(OH)_4$ units, followed by geometry optimization. **Figure 1d** shows the resulting structure of $Zr(OH)_4$. The initial cell sizes were 14.4 × 14.4 × 9.5 $Å^3$ (determined from the experimental crystal structure of *t*-ZrO_2[20]). MD simulation in the NPT ensemble was performed for 10 ps under ambient conditions (25 ˚C and 1 bar). The time constants of the thermostat[21-23] and barostat[24] were 500 fs, and the simulation time step was 0.5 fs. **Figure 1e** shows the equilibrated $[Zr(OH)_4]_{32}$ obtained by the MD simulation in the NPT ensemble for 10 ps. The mean cell lengths in the last 5 ps of the trajectory were $L_x \times L_y \times L_z = 15.3 \times 15.3 \times 11.1$ $Å^3$. MD simulation in the NVT ensemble was performed for 10 ps using the mean cell lengths, and the RDF was computed using snapshots in the trajectory every 4 fs.

2.2.2 *am*-ZrO_2

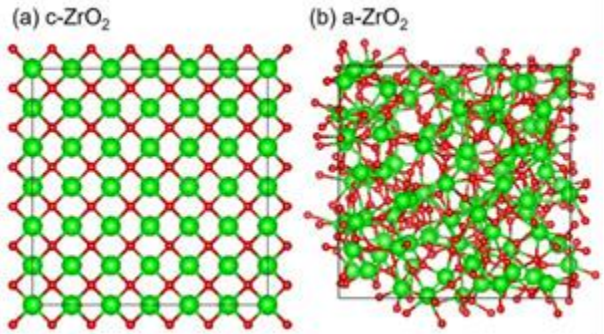

Figure 2. (a) Cubic ZrO_2 and (b) prepared amorphous ZrO_2 (*am*-ZrO_2) in the bulk phase. The black lines represent the boundaries of a periodic boundary condition.

We next prepared bulk *am*-ZrO_2 and its surface by thermal annealing with AIMD simulations.[25, 26] The initial configuration was 3 × 3 × 3 unit cells of the experimental cubic ZrO_2[27] crystal shown in **Figure 2a**, resulting in the chemical formula $Zr_{81}O_{162}$. First, to melt zirconia, the crystal structure was melted by MD simulation at 4000 K for 4 ps in an NPT ensemble at ambient pressure (1 bar). The time constants of both the thermostat[21-23] and barostat[24] were 500 fs, and the simulation time step was 2 fs. Second, the bulk ZrO_2 was cooled down in stages by changing the temperature to 3600, 3200, · · ·, 800, 400, 298 K (25 °C) with 400 K decrement, and at each temperature the MD simulation was conducted for 1 ps. Afterwards, MD simulation at ambient temperature (25 °C) was performed for 5 ps, and the mean cell length was 16.8 Å. The resulting density is 4.71 g/cm^3, which is slightly larger than the experimental value of 4.47 g/cm^3.[28] With the cell length, we performed the MD simulation in the NVT ensemble for 10 ps after an equilibration run for 10 ps, and the radial distribution function was calculated using the snapshots in the trajectory every 16 fs. **Figure 2b** shows a snapshot of the MD simulation.

The *am*-ZrO_2 surface was cleaved from the prepared bulk *am*-ZrO_2 and the geometry of the surface was optimized. After the geometry optimization, because the cleaved surface was not well annealed, MD simulation of equilibration for 8 ps at 300 °C (experimental reaction temperature[1] and calcination temperature[29, 30]) followed. The surface geometry was optimized and used to compute the adsorption energy on the *am*-ZrO_2 surface. To obtain the distribution of adsorption energy, adsorbates were adsorbed to (at least) 10 surface Zr atoms.

To evaluate the surface OH concentration, we performed an MD simulation of the *am*-ZrO_2/water interface, because the surface OH group can play an important role in various chemical processes such as adsorption.[31] The starting geometry for 64 H_2O was from pure liquid water[32] in the bulk phase and was optimized to the cell lengths of $L_x \times L_y \times L_z = 16.8 \times 16.8 \times 6.0$ Å^3. The water slab was placed on the ZrO_2 slab, and the geometry was optimized by decreasing L_z to 21.8 Å. Starting from the optimized interface, MD simulation at 300 °C was performed for 10 ps in the NVT ensemble. Afterwards, we removed all water molecules that were not dissociated from the interface and ran the annealing MD simulations again to compare with experiment since in experiment *am*-ZrO_2 was calcined at 673 K.[9] Starting from the optimized surface, MD simulation at 400 °C was performed for 10 ps in the NVT ensemble. Subsequently, the *am*-ZrO_2 surface was optimized and the adsorption energy was calculated.

2.2.3 *t*-ZrO_2

To compare the surface properties of crystalline zirconia with those of the *am*-$Zr(OH)_4$ and *am*-ZrO_2 surfaces, we prepared *t*-ZrO_2 surfaces with supercell sizes similar to those of the amorphous surfaces explained above. The initial geometry of a tetragonal zirconia in the bulk phase was generated by a periodic 2 × 2 × 1 (Zr_8O_{16}), 3 × 3 × 2 ($Zr_{36}O_{72}$), and 4 × 4 × 3 ($Zr_{96}O_{192}$) supercells of bulk *t*-ZrO_2 unit cell determined experimentally.[20] For each supercell, the cell lengths were isotropically scaled, and the geometry was optimized. This optimization was repeated until the total energy reached its minimum value.

In the calculations of the surface and adsorption energies, we cleaved the five low-index facets of *t*-ZrO_2(101), (001), (100), (111), and (110) surfaces from the bulk zirconia. A previous DFT study[33] demonstrated that these surfaces exhibited low surface energies, and therefore, high

surface stability. The slab consisted of 96 formula units (ZrO_2) for the (101), (001), and (100) surfaces, 120 formula units for the (111) surface, and 108 formula units for the (110) surface. The cell length along the surface normal direction was more than 35.00 Å; hence, the length of the vacuum region was more than 12 Å. **Table S1** summarizes cell lengths *a* and *b* along the parallel surface direction.

To examine the surface OH density at the *t*-ZrO_2(101) surface (most stable surface[33]), we optimized the geometry of the water interface with 64 water molecules with the initial configuration from our previous work,[32] and performed MD simulations for 5 ps for an equilibration run and 5 ps for a production run at 300 °C, considering that the calcination temperature was higher than 573 K.[9] In this MD simulation, the bottom ZrO_2 layer was fixed to the bulk structure. Here, the time constant of thermostat[21-23] was 1 ps.

2.2.4 *m*-ZrO_2

We employed similar computational conditions for *m*-ZrO_2 and *t*-ZrO_2. The initial geometry of the supercell for bulk *m*-ZrO_2 was generated using periodic 2 × 2 × 2 ($Zr_{32}O_{64}$), 3 × 3 × 3 ($Zr_{108}O_{216}$), and 4 × 4 × 4 ($Zr_{256}O_{512}$) supercells. The cell lengths were optimized, as in the case of *t*-ZrO_2.

The *m*-ZrO_2 surfaces were cleaved from the bulk phase, and **Table S1** summarizes the cell lengths of the five facets of *the m*-ZrO_2(111), (101), (011), (110), and (111) surfaces, which exhibited low surface energies, and therefore, a high surface stability.[34] The cell length along the *c* direction was 35 Å, so that the length of the vacuum region was more than 12 Å. The chemical

formula of the surface supercell is $Zr_{80}O_{160}$ for the (111) surface and $Zr_{96}O_{192}$ for the other surfaces.

A water interface was also prepared to measure the surface OH density as for *t*-ZrO_2: 64 water molecules[32] were placed on top of the *m*-ZrO_2(111) surface (the most stable surface), and the geometry was optimized with the bottom ZrO_2 layer fixed to the structure in the bulk phase. Afterwards, the MD simulation was performed for 5 ps for an equilibration run and 5 ps for a production run at 573.15 K.

3 Results

3.1 Experimental results

To understand the CO_2 adsorption properties, we prepared three types of ZrO_2 named: Zr-1, Zr-2, and Zr-3. We used X-ray diffraction (XRD) to study the structure of each sample and confirmed that Zr-1 was amorphous, Zr-2 was mainly tetragonal, and Zr-3 was monoclinic (**Figure S1**). **Table 1** lists the surface areas and pore volumes of each sample. Zr-1 had a higher specific surface area (206 $m^2\ g^{-1}$) than the other types of ZrO_2 (~ 80 $m^2\ g^{-1}$).

Table 1 Specific surface area, pore volume, and CO_2 desorption for ZrO_2.

Sample	Main crystal phase	SSA*	Pore volume	CO_2 desorption		Total CO_2 desorption	
				Temp.	Amount		
		[$m^2\ g^{-1}$]	[$cm^3\ g^{-1}$]	[℃]	[μmol m^{-2}]	[μmol m^{-2}]	[mmol g^{-1}]
Zr-1	Amorphous	206	0.17	142	6.9	13	2.8
				198	3.9		

				255	2.8		
Zr-2	Tetragonal	73	0.17	148	13	30	2.2
				230	8.0		
				305	6.3		
				409	3.0		
Zr-3	Monoclinic	87	0.48	133	12	24	2.1
				190	8.0		
				249	4.4		

* Specific surface area.

We conducted an experiment to investigate how CO_2 desorbed from different types of ZrO_2 surfaces at elevated temperatures. **Figure 3** shows the CO_2-TPD profiles. The high-temperature peak represents CO_2 desorption from sites with high basicity because CO_2 is acidic. According to literature,[35] peaks at < 200 °C, ~ 300 °C, and > 300 °C are attributed to CO_2 desorption from weak, moderate, and strong basic sites, respectively. For example, three peaks for Zr-1 were observed at 133, 198, and 249 °C. In addition, the peak area was proportional to the amount of CO_2 desorption.

The results for Zr-1 and Zr-3 were compared. The peak positions were similar, indicating that both ZrO_2 samples had similar basic sites. The difference in the results is the CO_2 desorption amount per unit specific surface area: the amount of Zr-1 (13 μmol m^{-2}) was much smaller than that for Zr-3 (24 μmol m^{-2}), as shown in **Table 1**. Therefore, the number of basic sites on *am*-ZrO_2 is much smaller than that on *m*-ZrO_2. Next, the results for Zr-3 and Zr-2 are compared. Only Zr-2 exhibited several peaks at >300°C, attributed to CO_2 desorption from strong basic sites. Therefore, *t*-ZrO_2 possesses sites with higher basicity than *m*-ZrO_2 and *am*-ZrO_2.

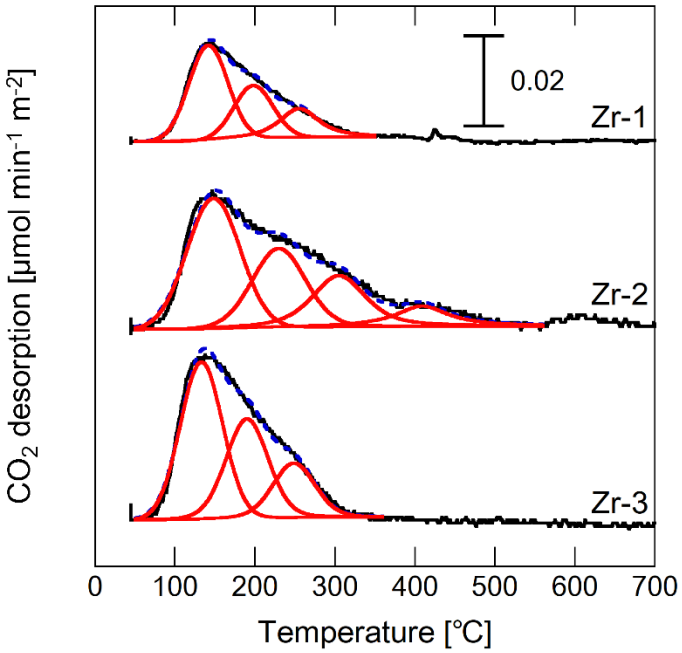

Figure 3 CO_2-TPD profiles of Zr-1, Zr-2, and Zr-3. Black solid line: raw data. Blue dotted line: peak sum. Red solid line: separated peak.

3.2 Structure of Bulk Zirconia

3.2.1 *am*-$Zr(OH)_4$

The resulting density of bulk *am*-$Zr(OH)_4$ by our MD simulations in **Section 2.2.1** is 3.27 g/cm^3 and it agrees with the experimental value of 3.25 g/cm^3.[36] Five water molecules spawned by condensation of hydroxyl groups during the MD simulation as shown in Scheme 1:

$$2Zr(OH)_4 \rightarrow (OH)_3Zr{-}O{-}Zr(OH)_3 + H_2O$$

Scheme 1: Dehydration of Zirconium(IV) hydroxide.

The condensation yields the O/Zr atomic ratio of (32 × 4 − 5)/32 = 3.84, which is close to the experimental value of 3.28 determined by the X-ray photoelectron spectroscopy (XPS) technique.[37]

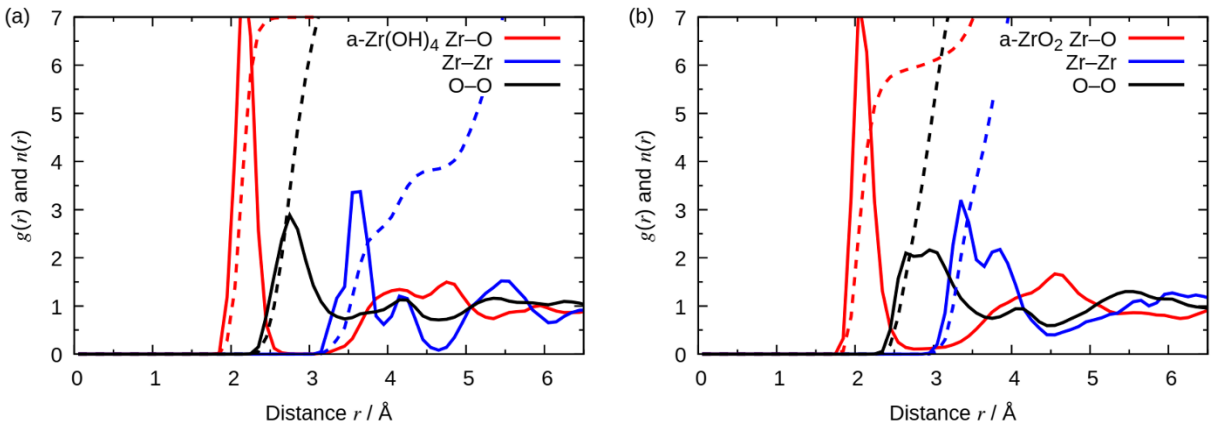

Figure 4. Radial distribution function *g* (solid line) and coordination number *n* (dashed line) of the Zr–O (red), Zr–Zr (blue), and O–O (black) atomic pairs in (a) *am*-$Zr(OH)_4$ and (b) *am*-ZrO_2.

Figure 4a shows the radial distribution function (RDF) of *am*-$Zr(OH)_4$ O, Zr–Zr, and O–O atomic pairs. The peak with the shortest distance among all the RDFs arises from the Zr−O atomic pair. The peak has its greatest intensity around 2.15 Å in agreement with 2.15 Å determined by the X-ray structure analysis[7] and 2.11 Å determined by the extended X-ray absorption fine structure (EXAFS) spectrum of an aqueous zirconium hydroxide colloid.[38] The agreement confirms the reproducibility of *am*-$Zr(OH)_4$ in our MD simulations. Next, there are broader peaks around 2.5−3.0 Å that correspond to the O−O distances. The next two peaks at

3.47 and 4.0 Å come from the Zr−Zr atomic pairs. The coordination number (also shown in **Figure 4a** by dashed lines) of the Zr−Zr pair in the first coordination shell is approximately four, which is slightly different from the experimental measurement (4.82 for two-dimensional sheets.[7]

3.2.2 *am*-ZrO_2

Figure 4b shows the RDF of bulk *am*-ZrO_2 for Zr−O, Zr−Zr, and O−O atomic pairs. To compare the results with the experiment by X-ray scattering,[28] **Table 2** lists the peak positions of the first to third peak positions in the RDFs for Zr−O, Zr−Zr, and O−O atomic pairs. Overall, the computed positions are in good agreement with the experiment.[28] The coordination number is approximately 6 in the first coordination shell (up to approximately 3 Å), which is consistent with the proposed ZrO_6 octahedra.[28] Though a minor disagreement can be noticed for the O−O pair (especially in the second and third peaks), the agreement of the peak positions indicates that the simulated bulk *am*-ZrO_2 reproduces the experimental structure of *am*-ZrO_2.

Table 2. First−third peak positions (in Å) of *am*-ZrO_2 by our MD simulation and X-ray scattering. [28]

pair	Zr−O			Zr−Zr			O−O		
	1st	2nd	3rd	1st	2nd	3rd	1st	2nd	3rd
MD	2.06	3.93	4.59	3.43	3.82	3.95	2.84	4.12	5.42

Exp.	2.14	4.27	4.65		3.41	3.71	3.98		2.96	3.98	4.86

3.2.3 *t*-ZrO_2

Table S2 summarizes the optimized cell lengths, which converge within an error of 0.1 Å for $n_a \times n_a \times n_a = 4 \times 4 \times 3$ (n is the number of unit cells in a supercell). The converged cell lengths (a = 3.618 Å and c = 5.220 Å for a unit cell) differ slightly from a = 3.613 Å and c = 5.235 Å in the previous DFT study[10] and the experimental values of a = 3.612 Å and c = 5.212 Å,[20] mainly because of the different computational conditions, such as the larger supercell in this study.

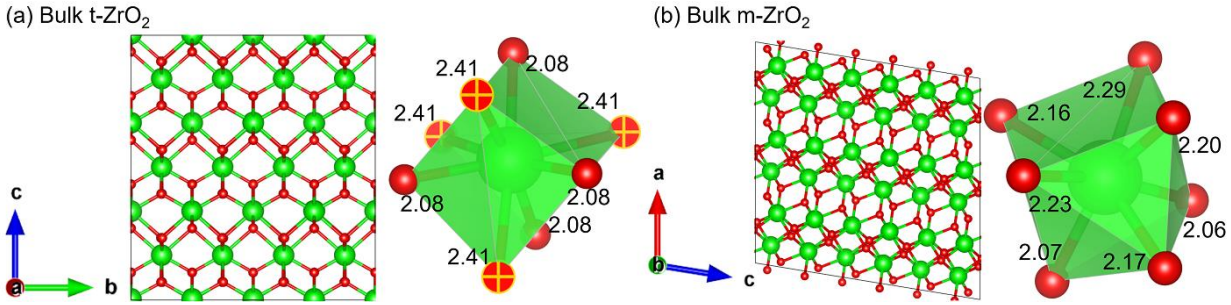

Figure 5. Structures of bulk (a) *t*-ZrO_2 and (b) *m*-ZrO_2, and the corresponding ZrO_8 and ZrO_7 cluster, respectively. The values in the ZrO_x cluster show the Zr−O bond lengths in Å. The yellow crosses in the ZrO_8 cluster of (a) denote the longer Zr−O bond. Color code: green, Zr; red, O.

Figure 5a shows the structure of the bulk *t*-ZrO_2 and the representative ZrO_8 cluster. The Zr atom in bulk *t*-ZrO_2 has eight Zr−O bonds. The eight Zr−O bonds are classified into two groups: the Zr−O bond lengths of the four bonds are 2.08 Å and those of the other bonds are 2.41 Å on an average. The corresponding experimental Zr−O distances are 2.09 and 2.39 Å,[20] respectively, which are close to our results.

3.2.4 *m*-ZrO_2

Table S3 lists the optimized cell lengths of the bulk *m*-ZrO_2. The cell length converged for the $3 \times 3 \times 3$ ($Zr_{108}O_{216}$) supercell; therefore, the energy of this supercell was employed to calculate the surface energy. The optimized cell lengths (a = 5.167, b = 5.230 Å) were comparable to the experimental results, a = 5.145, b = 5.208 Å,[39] and a = 5.169, b = 5.232 Å[40], and the previous theoretical results, a = 5.145, b = 5.207 Å.[34]

Figure 5b shows the bulk structure of *m*-ZrO_2 and a representative ZrO_7 cluster. Each Zr atom in bulk *t*-ZrO_2 has seven Zr−O bonds: three bonds with O_{3c} with shorter bond lengths (2.06−2.17 Å, and four bonds with O_{4c} with 2.16 and 2.29 Å. The agreement between the calculated lattice parameters of *m*-ZrO_2 and the corresponding experimental values indicates the adequate accuracy of our DFT calculations. We note that the Zr−O bond lengths in crystalline ZrO_2 are slightly larger than in *am*-ZrO_2 that has a peak at 2.05 Å in RDF (**Figure 4**), suggesting the stronger Zr−O bonds in bulk *am*-ZrO_2.

3.3 Surface Energy and Structure

3.3.1 *am*-$Zr(OH)_4$

The surface energy of *am*-$Zr(OH)_4$ is as low as 0.32 J/m^2, which is much lower than those at the crystal ZrO_2 surfaces, such as 1.06−1.69 J/m^2 at the *t*-$ZrO_2(101)$[33, 41, 42] surface (discussed below). This is because each $Zr(OH)_4$ tetramer is bound by hydrogen bonds, whereas at the *am*-ZrO_2 and crystalline surfaces, Zr−O covalent bonds are broken to form their surface. This indicates that *am*-$Zr(OH)_4$ exposes its surface much more easily than crystalline ZrO_2, and this leads to much smaller *am*-$Zr(OH)_4$ particles (0.5−2.8 nm[9, 38]) than crystal ZrO_2 (approximately 4−50 nm [43 44]), as demonstrated by the experimental measurements.

Next, we calculate the number of Zr−O bonds that can indicate how much Zr atoms is unsaturated at the *am*-$Zr(OH)_4$ surface using the trajectory in the MD simulation at 300 °C. For this calculation, we defined the Zr−O bond if the bond length was smaller than 3.1 Å, which is the default threshold value in VESTA.[17] The average number of Zr−O bonds is 7.00 in bulk and remains 6.97 at surface. This is almost the same as 7.00 in *m*-ZrO_2, yet smaller than 8 in *t*-ZrO_2. These results indicate that the coordinatively unsaturated Zr^{4+} sites (cus-Zr^{4+})[45, 46] are rare on the *am*-$Zr(OH)_4$ surface because the surface OH groups cover the surface almost completely.

3.3.2 *am*-ZrO_2

The surface energy of *am*-ZrO_2 is 0.57 J/m^2, which is slightly larger than that of the *am*-$Zr(OH)_4$ surface, but smaller than crystalline surfaces as discussed below. This indicates that the *am*-ZrO_2 surface can be cleaved more easily than the crystalline surfaces. This result is consistent with the absence of sharp diffraction peaks in the XRD patterns,[1] indicating that the nanoparticles were smaller than *t*-ZrO_2 and *m*-ZrO_2. [43 47]

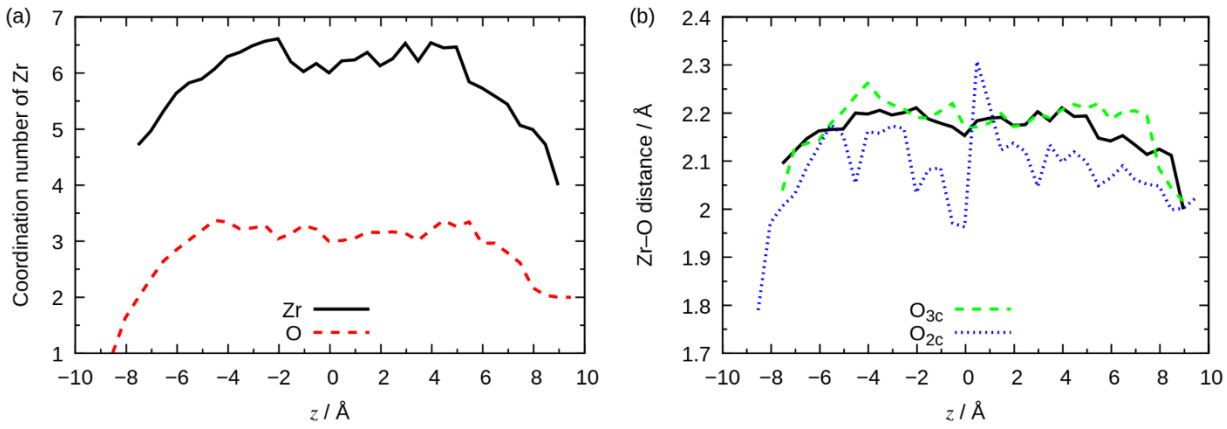

Figure 6. Average (a) coordination number of Zr and O atoms and (b) Zr−O distance along the surface normal direction at the *am*-ZrO_2 surface. The distribution of the Zr−O distance (black solid line) is further decomposed into the contributions from a 3-fold coordinated O site (O_{3c}; green dashed line) and a 2-fold coordinated O site (O_{2c}; blue dotted line). z = 0 Å indicates the center of the slabs.

To understand the number and strength of Zr−O bonds, **Figure 6** shows the average coordination numbers of Zr and O atoms and the Zr−O distance at *am*-ZrO_2 surface using the trajectory from the MD simulation. The average coordination number of Zr atoms in *am*-ZrO_2 increases from ~4.5 at the surface to 6.0−6.5 in bulk, which is much smaller than that of 7 at the *t*-ZrO_2(101) surface, 6−7 at the *m*-ZrO_2($\bar{1}11$) surface, and 8 (*t*-ZrO_2) and 7 (*m*-ZrO_2) in bulk. This indicates that each Zr−O bond is stronger at *am*-ZrO_2 surface than at the crystalline zirconia surfaces. Similarly, the average coordination number of O atoms in *am*-ZrO_2 increases from ~2 at the surface to ~3 in the bulk. Accordingly, the Zr−O bond lengths gradually increases from ~ 2.1 Å at the surface to ~2.2 Å in bulk. Furthermore, when the bond length is divided into

contributions from a 3-fold coordinated O atom (O_{3c}) and a 2-fold coordinated O atom (O_{2c}), the bond length of O_{3c} is longer. This indicates that the number of O_{2c} atoms increases, and the Zr−O bonds become stronger at the *am*-ZrO_2 surface than in the bulk. We note that the results in **Figure 6** are not smooth because *am*-ZrO_2 is heterogeneous.

3.3.3 *t*-ZrO_2

Table 3. Surface energy γ (J/m^2), surface coordination number *N* of Zr atom at *t*-ZrO_2 and *m*-ZrO_2 surfaces.

	t-ZrO_2					*m*-ZrO_2				
	(101)	(001)	(100)	(111)	(110)	$(\bar{1}11)$	(111)	(110)	$(\bar{1}01)$	(011)
Γ	1.32	1.36	1.44	1.66	1.87	1.22	1.37	1.50	1.54	1.60
N	7	6	6	5−6	6	6−7	6	5	5−6	4−5

Table 3 summarizes the computed surface energies of the five low-index *t*-ZrO_2 surfaces: (101), (001), (100), (111), and (110). To calculate the surface energy, we employed the energy of bulk *t*-ZrO_2 with $n_a \times n_b \times n_c = 4 \times 4 \times 3$ ($Zr_{96}O_{192}$), as discussed in **Section 3.2.3**. The surface energy of the *t*-ZrO_2(101) surface is comparable to 1.06−1.69 J/m^2 in the previous DFT studies using the other DFT functionals.[10, 33, 41, 42] The relative surface energies qualitatively agree with

the previous calculations[33] and increase in the following order: (101) < (001) < (100) < (111) < (110). The surface energy is approximately proportional to the coordination number of the surface Zr atom, as listed in **Table 3**, although the (111) surface is an exception. The surface energy reaches a minimum for the (101) surface owing to the highest coordination number of seven, which is smaller than eight for bulk *t*-ZrO_2. As no surface reconstruction was observed, the surface stability was closely related to the coordination number. Owing to its high stability, the *t*-ZrO_2(101) surface was used in the following calculations for *t*-ZrO_2.

The surface Zr atoms at the *t*-ZrO_2(101) surface have only 7-fold coordination, whereas the top-most O atoms have a 3-fold coordination. The *t*-ZrO_2(101) surface was characterized by a specific bond length between Zr and O atoms. The topmost O_{3c} and Zr_{7c} atoms are classified into two types, as illustrated in **Figure 7**:[48, 49] one Zr (denoted by Zr_S hereafter) atom has three relatively long Zr−O bonds, and the other Zr (denoted by Zr_W) atom has three short Zr−O bonds. Zr_S and Zr_W sites are named after the strong and weak Lewis sites, as in the previous study.[48, 49] Accordingly, one O atom has two long and one short Zr−O bond, and the other O atom has two short and one long Zr−O bond. The characteristic short and long Zr−O bonds originate from the structure of the ZrO_8 cluster in the bulk phase, as discussed in **Section 3.2.3**. The long Zr−O bond suggests a facile structural rearrangement in chemical reactions such as adsorption, which will be discussed in **Section 3.5**.

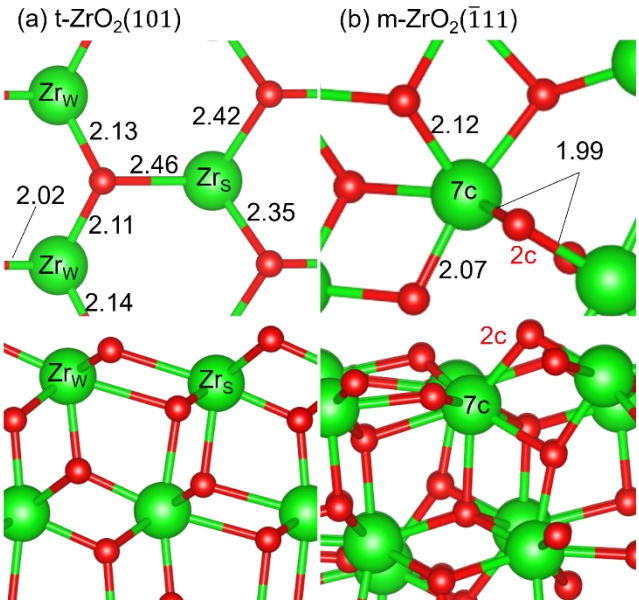

Figure 7. Top (top panels) and side (bottom panels) views of the top layer of the (a) *t*-ZrO_2(101) and (b) *m*-$ZrO_2(\bar{1}11)$ surfaces. The bond lengths in Å and atomic labels are also displayed. $Zr_{W/S}$ respectively indicates the weak/strong Lewis sites, [48, 49] and 7c (2c) denotes seven- (two-) fold coordination.

3.3.4 *m*-ZrO_2

Table 3 lists the surface energies of the *m*-$ZrO_2(\bar{1}11)$, (111), (011), (110), and (111) surfaces. To calculate the surface energy, we employed the results for $n_a \times n_b \times n_c = 3 \times 3 \times 3$ ($Zr_{108}O_{216}$) discussed in **Section 3.2.4**. As in the case of *t*-ZrO_2, the surface energy was approximately proportional to the coordination number of the surface Zr atom and the minimum for the $(\bar{1}11)$ surface owing to the highest coordination number. The computed surface energy at the $(\bar{1}11)$ surface is close to 0.76−1.22 J/m^2 in the previous works[34, 50-52] that employed the different computational conditions. The maximum coordination number of 7 for the $(\bar{1}11)$ surface is also

the same as that for bulk *m*-ZrO_2; therefore, this surface is the most stable. Thus, only the $(\bar{1}11)$ surface was employed as the *m*-ZrO_2 surface in the following calculations. It is to be noted that, at the $(\bar{1}11)$ surface, most O atoms have a 3-fold or 4-fold coordination, and 3/4 of the Zr atoms are Zr_{6c} and 1/4 of the Zr_{7c} atoms lie beside O_{2c} (**Figure 7b**).[33] Furthermore, the O_{3c} atoms have bond lengths ranging from 2.07 to 2.29 Å, and the O_{2c} atoms has a shorter Zr−O bond length of 1.99 Å.

The surface Zr sites were only seven-coordinated on the *t*-ZrO_2(101) surface. On the other hand, the percentages of 4-, 5-, 6-, and 7-coordinated surface Zr atoms were 0, 0, 75, and 25% at *m*-$ZrO_2(\bar{1}11)$ surface and 11, 33, 39, and 17% at *am*-ZrO_2 surface, respectively. Thus, the coordination environment of the Zr atoms at *m*-$ZrO_2(\bar{1}11)$ surface was closer to that at the *am*-ZrO_2 surface.

3.4 Surface OH Density

To understand the impact of the surface OH groups on molecular adsorption, we compared the surface OH densities at *am*-$Zr(OH)_2$ and hydroxylated *am*-, *t*-, *m*-ZrO_2 surfaces summarized in **Table 4**, in which adsorbates are classified into terminal OH, bridged OH, and water. **Figure 8** shows the *am*-$Zr(OH)_4$ and hydroxylated ZrO_2 surfaces.

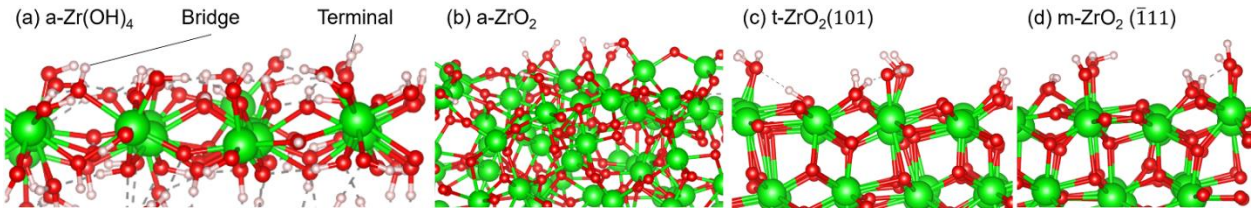

Figure 8. Side views of (a) *am*-$Zr(OH)_4$, hydroxylated (b) *am*-ZrO_2, (c) *t*-ZrO_2, and (d) *m*-ZrO_2 surfaces. The chemisorbed water molecules (which did not split into H + OH) are not displayed for clarity.

3.4.1 *am*-Zr(OH)$_4$

Table 4. Surface densities of terminal OH, bridged OH, and chemisorbed water in nm^{-2} at zirconia surfaces.

	am-$Zr(OH)_4$	*am*-ZrO_2	*t*-ZrO_2(101)	*m*-$ZrO_2(\bar{1}11)$
Terminal OH	4.72	2.85	3.26	2.78
Bridged OH	3.86	7.82	3.26	2.78
Water	0.86	4.27	1.63	3.89

The number of terminal, bridged OH, and adsorbed water molecules exposed at the *am*-$Zr(OH)_4$ surface are 4.93, 18.23 and 3.43 OH/nm^2, respectively. This is comparable to the terminal and bridged hydroxyl densities of 7.98 and 26.5 μmol/m^2 = 4.8 and 16.0 OH/nm^2 without calcination determined by the nuclear magnetic resonance (NMR) study.[53] The computed bridged/terminal ratio of our $Zr(OH)_4$ slab is 3.7. This is larger than 2.6 estimated by XPS spectra,[29] comparable to 3.3−3.7 by NMR spectroscopy,[53] and smaller than 4.1−5.5 by DFT calculations.[4] The

computed surface OH density at the *am*-$Zr(OH)_4$ surface belongs to the high-value category among *am*-, *m*-, and *t*-ZrO_2, which range from 1.6 to 9.4 OH/nm^2 experimentally.[9] Thus, the *am*-$Zr(OH)_4$ surface is covered by the surface OH groups.

3.4.2 *am*-ZrO_2

At the prepared *am*-ZrO_2/water interface, 4.27 OH/nm^2 water molecules were chemisorbed on cus-Zr^{4+} (Zr^{4+}−OH_2). The terminal and bridge OH concentrations were 2.85, 7.82 OH/nm^2, respectively. The computed surface OH density differs from the IR spectroscopy results that reported the OH density of 2.1 OH/nm^2 for ZrO_2 calcined at 673 K.[9] Considering the high calcination temperature of 673 K, the difference is reasonable: the desorption energy at the ZrO_2 surface is at most 0.77 eV (see below). This indicates that most surface OH groups vaporize at high temperatures, considering that the Redhead equation[54] yields a desorption temperature of 673 K corresponds to 1.91 eV.

3.4.3 *t*-ZrO_2

The experimental surface density of the OH groups was 3.5 OH/nm^2 for *t*-ZrO_2 at a calcination temperature of 1323 K, as measured by IR spectroscopy,[9] which corresponds to the sum of the terminal and bridged OH groups in our MD simulations because water molecules evaporate and OH groups remain at the surface after calcination. The computed surface density of the corresponding OH groups in **Table 4** at the *t*-ZrO_2(101) surface is 1.63 + 3.26 = 4.89 OH/nm^2. This is slightly larger than the experimental value because our MD simulation neglects the effect of water evaporation during calcination, which requires a long simulation time. All the terminal OH groups were attached to the Zr_S sites. After adsorption to the Zr_S site, water molecules are easily split into a terminal OH and protonate the nearby O_{3c} site. Among the bridged OH groups,

50% were attached to the O_{3c} atom (bibridged OH [9] shown in **Figure S2b**), while 50% were attached to the O_{2c} atom (tribridged OH [9] shown in **Figure S2c**). In addition, 88% of Zr_S sites are occupied by adsorbates, whereas only 25% of Zr_W sites are occupied by adsorbates, indicating that Zr_S sites are stronger Lewis sites.[48, 49]

3.4.4 *m*-ZrO_2

The computed surface OH density (terminal + bridged) is 5.56 OH/nm^2 that is within the experimental range of 3.2−9.4 OH/nm^2 depending on the calculation temperature and preparation conditions.[9, 55] In addition, all of O_{2c} forms a bibridged OH group. No adsorbate exists on all Zr_{7c} sites, whereas terminal OH groups or water molecules adsorb on all Zr_{6c} sites next to the O_{2c} site. These findings suggest that the Zr_{7c} and Zr_{6c} sites are chemically inactive and active, respectively.

3.5 Adsorption Energy

Figure 9 lists the adsorption energy of CO_2 on zirconium compounds and shows their structures.

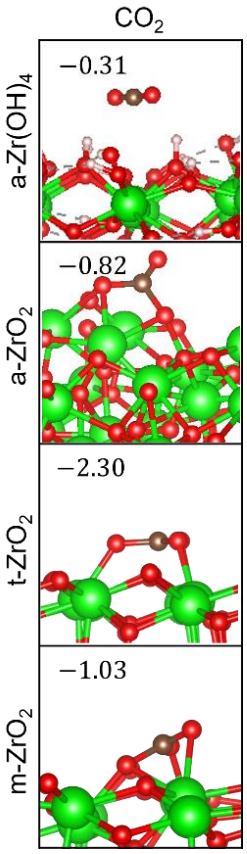

Figure 9. Optimized structures of adsorbed CO_2 at the *am*-$Zr(OH)_4$ (first row), *am*-ZrO_2 (second row), *t*-ZrO_2(101) (third row), and *m*-$ZrO_2(\bar{1}11)$ (fourth row) surfaces. The corresponding adsorption energy is also shown in the unit of eV.

3.5.1 *am*-$Zr(OH)_4$

The computed adsorption energy of CO_2 (−0.31 eV) is much higher than that on ZrO_2 crystalline surfaces (for instance, −1.00 eV at *t*-ZrO_2(101) surface[10]). This is because CO_2 is not adsorbed as a carbonate species on the surface, as shown in **Figure 9**. In addition, the surface has high hydrophilicity resulting from a large number of hydroxyl groups, that is, it has many hydrogen

bonds among the OH groups. Therefore, during adsorption, CO_2 molecules must break the hydrogen bonds at the surface.

3.5.2 *am*-ZrO_2

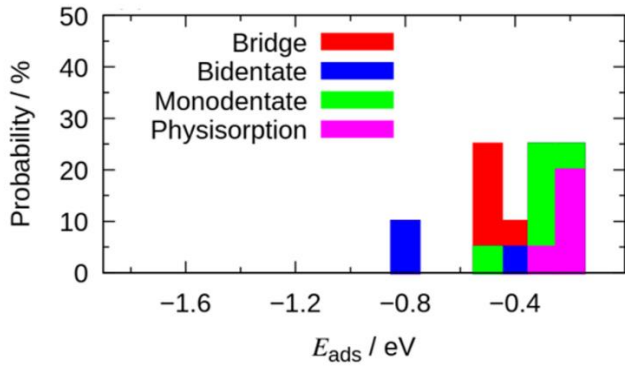

Figure 10. Probability distribution of adsorption energy of CO_2 at the *am*-ZrO_2 surface.

Figure 10 shows a histogram of the adsorption energies on the *am*-ZrO_2 surface. The broad distribution indicates heterogeneity of the *am*-ZrO_2 surface and molecular adsorption. The distribution of CO_2 in **Figure 10** is further decomposed into bridge, bidentate, monodentate, and physisorption, and the former two adsorptions are stronger than the latter two. **Figure 9** summarizes the most stable structures, and other adsorption species are shown in **Figure S8** including the adsorption energy. CO_2 was most stably adsorbed as a bidentate carbonate species on Zr_{5c} and O_{2c} sites on the *am*-ZrO_2 surface (**Figure 9**), yet no stable polydentate carbonate species were found. **Figure 10** indicates that the lowest adsorption energy ($E_{ads} = -0.82$ eV) is larger than that on crystalline surfaces ($E_{ads} = -2.30$ eV and -1.03 eV). In addition, the

majority of the adsorption energies of CO_2 molecules on *am*-ZrO_2 were larger than the minimum value ($E_{ads} = -0.82$ eV). Therefore, the adsorption is not so strong as at crystalline surfaces, which agrees with the experimental findings.[45] The experimental results of CO_2-TPD showed a broad peak at *ca*. 140 °C [6] (**Table 1**), which corresponds to the adsorption energy of 1.2 eV according to the Redhead equation.[54] The previous experimental study [50] also reports a slightly smaller yet similar value of 95 kJ/mol = 0.99 eV for the *am*-ZrO_2 surface, which are closer to our theoretical result.

The computed numbers of surface Zr sites per surface area of *am*-, *t*-, and *m*-ZrO_2 surfaces were 6.9, 8.7, and 8.9 nm^{-2}, respectively. Multiplying the numbers with the specific surface area (SSA) in **Table 1** gives the numbers of surface Zr sites of 1.4×10^{21} g^{-1} (*am*-ZrO_2), 6.4×10^{20} g^{-1} (*t*-ZrO_2), and 7.7×10^{20} g^{-1} (*m*-ZrO_2). These results indicate that, although the number of surface Zr sites on *am*-ZrO_2 is larger than that on crystalline surfaces, fewer surface Zr sites adsorb CO_2 molecules and the amount of adsorbed CO_2 is smaller, as shown in **Table 1**.

3.5.3 *t*-ZrO_2

A CO_2 molecule adsorbs as a polydentate carbonate species on the *t*-ZrO_2(101) surface with three Zr−O bond lengths of 2.10, 2.10, and 2.11 Å between CO_3^{2-} and surface Zr atoms. The polydentate carbonate species replaced the position of the surface O atom with two long and one short Zr−O bond, as discussed in **Section 3.3.3**.

3.5.4 *m*-ZrO_2

A CO_2 molecule adsorbs as a polydentate carbonate species (**Figure 9**) on the *m*-$ZrO_2(\bar{1}11)$ surface and forms bonds with Zr_{7c}–O_{2c}–Zr_{6c} and nearby Zr_{6c}. This adsorption was stronger than that on *am*-ZrO_2, which is consistent with the experimental results.[56]

4 Discussion

4.1 Charge Distribution and Density of States

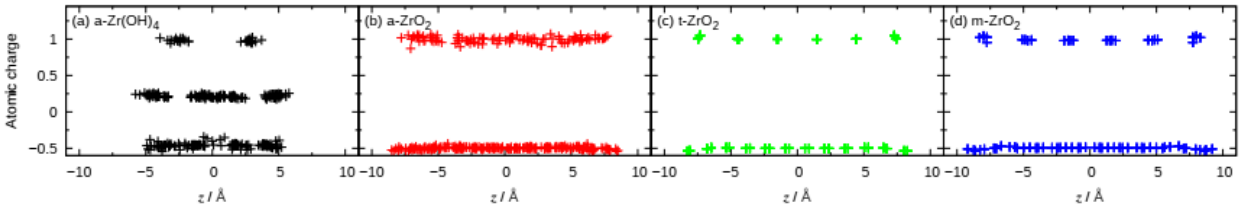

Figure 11. Charge distribution along the surface normal direction at the (a) *am*-$Zr(OH)_4$, (b) *am*-ZrO_2, (c) *t*-$ZrO_2(101)$, and (d) *m*-$ZrO_2(\bar{1}11)$ surfaces. z = 0 Å indicates the center of the slabs.

For analysis of the charge distribution in zirconia surfaces, **Figure 11** shows the plot of the atomic charges at the *am*-$Zr(OH)_4$, *am*-ZrO_2, *t*-$ZrO_2(101)$ and *m*-$ZrO_2(\bar{1}01)$ surfaces as a function of the depth coordinate along the surface normal direction. The positive (~1.0) and negative (∼–0.5) charges correspond to the charges of Zr and O atoms by Hirshfeld analysis,[57] respectively. In *am*-$Zr(OH)_4$, the charges of the H atoms are approximately +0.25. Although the charges at *am*-ZrO_2 surface slightly fluctuate compared to the crystalline ZrO_2 surfaces, the

behavior of the charges is almost the same, and the absolute value rises slightly as it approaches the surface. This indicates that Zr and O atoms are slightly more polarized than in the bulk, and there is little difference in the charge environment between the amorphous and crystalline surfaces.

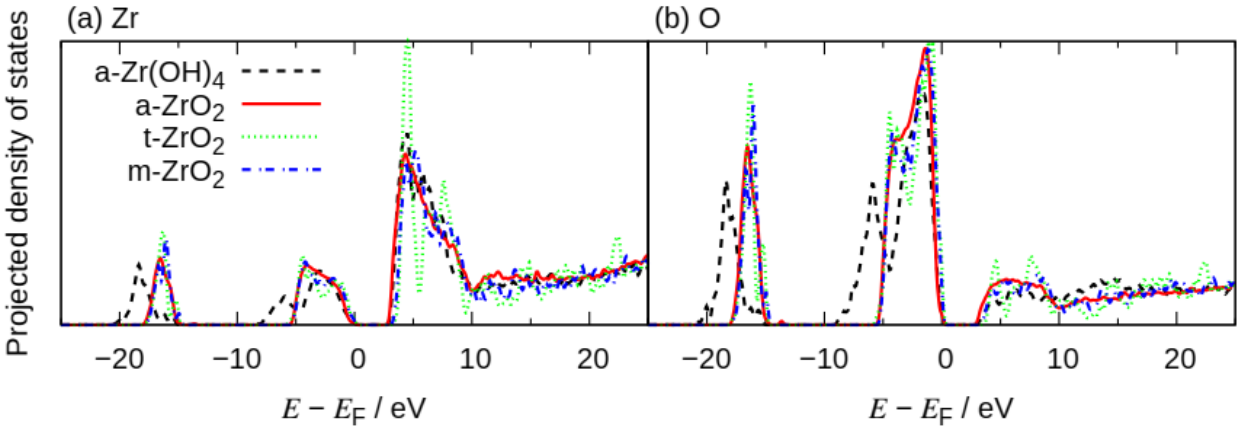

Figure 12. Projected density of states (PDOS) onto the orbitals of (a) Zr and (b) O atoms at *am*-$Zr(OH)_4$ (dash), *am*-ZrO_2 (solid), *t*-ZrO_2 (dot), and *m*-ZrO_2 (dash-dot) surfaces.

Figure 12 shows the projected density of states (PDOS) of Zr and O atoms at *am*-$Zr(OH)_4$, *am*-ZrO_2, *t*-ZrO_2(101), and *m*-$ZrO_2(\bar{1}11)$ surfaces. Although a slight difference in the PDOS at the *am*-$Zr(OH)_4$ surface can be seen, the results are qualitatively very similar in the four phases. The case of *am*-$Zr(OH)_4$ is exceptional in this comparison because the substrate has a different atomic composition and more surface OH groups.

The band gaps are also quite similar for the four phases: 3.20 eV (*am*-$Zr(OH)_4$), 3.05 eV (*am*-ZrO_2), 3.56 eV (*t*-ZrO_2), and 3.45 eV (*m*-ZrO_2). The computed band gaps are smaller than the experimental band gaps of 3.6−5.1 eV.[58] It is to be noted that the use of hybrid functional (PBE + 10.5% Hartree-Fock exchange that reproduced the band gap in anatase TiO_2[59, 60]) increase the computed band gap to better agree with the experiment as shown in **Figure S7**: 4.14 eV (*am*-$Zr(OH)_4$), 3.57 eV (*am*-ZrO_2), 4.50 eV (*t*-ZrO_2), and 4.35 eV (*m*-ZrO_2). Nevertheless, the PBE functional can capture qualitative electronic properties. Thus, the difference in electronic structures is not a major reason for the different absorption strengths compared with the structural ones discussed in **Section 3.5**.

4.2 Effect of Hydroxylation at *am*-ZrO_2 Surface

Finally, we discuss the effect of hydroxylation on the *am*-ZrO_2 surface. **Figure 13** shows a histogram of the adsorption energy at the hydroxylated surface, and the most stable adsorption shown in **Figure 14** occurs at similar surface sites on the non-hydroxylated *am*-ZrO_2 surface. The adsorption energies for most species were also similar to those at the *am*-ZrO_2 surface, and the surface OH group did not help the adsorption. In addition, CO_2 is adsorbed on the surface as hydrogen carbonate (HCO_3^-), and the minimum adsorption energy is −0.84 eV. HCO_3^- can form a bridged structure (**Figure S9a**) and form hydrogen bonds with neighboring surface OH groups (**Figure S9b**). These findings indicate that hydrophobic CO_2 molecules adsorb mainly to the non-hydroxylated surface Zr sites yet form hydrogen carbonate species.

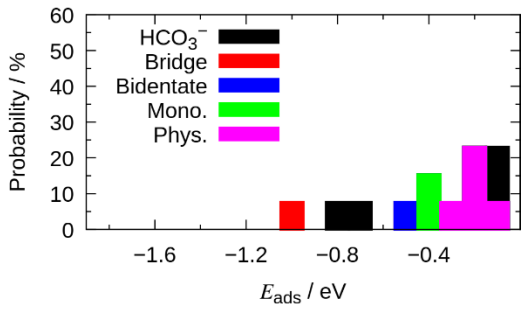

Figure 13. Probability distribution of adsorption energy of CO_2 at the hydroxylated *am*-ZrO_2 surface.

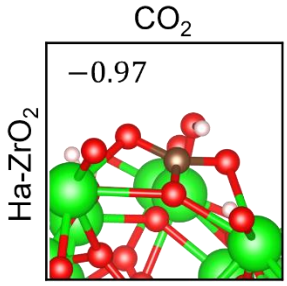

Figure 14. Optimized structures of adsorbed CO_2 at the hydroxylated a (Ha)-$Zr(OH)_4$ surface. The corresponding adsorption energy is also shown in the unit of eV.

5 Conclusions

Here, we studied the morphological dependence of molecular adsorption on zirconia surfaces to understand the origin of the weak adsorption of CO_2 on *am*-ZrO_2 compared to crystalline ZrO_2 using experiments and *ab initio* DFT calculations. XRD analysis and CO_2-TPD were performed to demonstrate the weaker adsorption of CO_2 on amorphous zirconia. Using DFT calculations,

am-$Zr(OH)_4$ and *am*-ZrO_2 were prepared via thermal annealing, and the resulting bulk structures were found to be consistent with the experimental results by comparing the RDFs and bulk density. In addition, the coordination number of Zr atoms and Zr−O bond lengths in bulk *am*-ZrO_2 were smaller than those in crystalline ZrO_2, indicating fewer and stronger Zr−O bonds. The surface structures of *am*-$Zr(OH)_4$, *am*-ZrO_2, and crystalline (*t*- and *m*-) ZrO_2, including the surface OH density, were systematically investigated. In addition, at the *am*-ZrO_2 surface, the average number and length of Zr−O bonds are much smaller than those in the crystalline ZrO_2. Despite the fewer Zr−O bonds and more undercoordinated Zr sites at the *am*-ZrO_2 surface, the Zr-O bonds at the *am*-ZrO_2 surface are stronger than those at the crystalline surfaces, which may be key to the weaker molecular adsorption. This is also because the charge environment and band structure of the zirconia surfaces in all phases remain almost the same. In addition, the strength of molecular adsorption at *am*-ZrO_2 surface showed a wide range of distributions, indicating the heterogeneity of the surface. The molecular mechanism of the specific adsorption capacity revealed in this study should be beneficial for applications, such as catalytic reactions at and adsorption of chemical compounds on *am*-ZrO_2 surface.

Supporting Information

The Supporting Information is available free of charge.

- si.pdf: XRD patterns of ZrO_2 samples, cell lengths, adsorption energy of the other molecules (H_2, H_2O, CH_3OH), PDOS by hybrid functional, and the other adsorption species of CO_2

- bulk-am-ZrOH4.cif and bulk-am-ZrO2.cif: cif files of bulk *am*-$Zr(OH)_4$ and *am*-ZrO_2, respectively.

- ZrOH4-surface.cif and am-ZrO2-surface.cif: cif files of *am*-$Zr(OH)_4$ and *am*-ZrO_2 surfaces, respectively.

Acknowledgement

This research was supported by JSPS KAKENHI, Japan (No. 21K04988), the NSG Foundation, the Iketani Science and Technology Foundation, TEPCO Memorial Foundation, and Iwatani Naoji Foundation. We used the supercomputer of the Institute for Solid State Physics, the University of Tokyo, ACCMS, Kyoto University under the Collaborative Research Program for Young Scientists, and Research Institute for Information Technology, Kyushu University.

References

(1) Tada, S.; Katagiri, A.; Kiyota, K.; Honma, T.; Kamei, H.; Nariyuki, A.; Uchida, S.; Satokawa, S. Cu Species Incorporated into Amorphous ZrO_2 with High Activity and Selectivity in CO_2-to-Methanol Hydrogenation. *J. Phys. Chem. C* **2018**, *122*, 5430-5442.
(2) Tada, S.; Kayamori, S.; Honma, T.; Kamei, H.; Nariyuki, A.; Kon, K.; Toyao, T.; Shimizu, K.-i.; Satokawa, S. Design of Interfacial Sites between Cu and Amorphous ZrO_2 Dedicated to CO_2-to-Methanol Hydrogenation. *ACS Catal.* **2018**, *8*, 7809-7819.
(3) Balow, R. B.; Lundin, J. G.; Daniels, G. C.; Gordon, W. O.; McEntee, M.; Peterson, G. W.; Wynne, J. H.; Pehrsson, P. E. Environmental Effects on Zirconium Hydroxide Nanoparticles and Chemical Warfare Agent Decomposition: Implications of Atmospheric Water and Carbon Dioxide. *ACS Appl. Mater.* **2017**, *9*, 39747-39757.
(4) Iordanov, I. O.; Bermudez, V. M.; Knox, C. K. Computational Modeling of the Structure and Properties of Zr(OH)4. *J. Phys. Chem. C* **2018**, *122*, 5385-5400.
(5) Oshima, K.; Honma, Y.; Kinoshita, K.; Gao, Z.; Honma, T.; Tada, S.; Satokawa, S. Mechanochemical Effect in Mixing Sponge Copper with Amorphous ZrO_2 Creates Effective

Active Sites for Methanol Synthesis by CO_2 Hydrogenation. *J. Phys. Chem. C* **2021**, *125*, 8155-8162.
(6) Yamamura, T.; Tada, S.; Kikuchi, R.; Fujiwara, K.; Honma, T. Effect of Sm Doping on CO_2-to-Methanol Hydrogenation of Cu/Amorphous-ZrO_2 Catalysts. *J. Phys. Chem. C* **2021**, *125*, 15899-15909.
(7) King, G.; Soliz, J. R.; Gordon, W. O. Local Structure of $Zr(OH)_4$ and the Effect of Calcination Temperature from X-ray Pair Distribution Function Analysis. *Inorg. Chem.* **2018**, *57*, 2797-2803.
(8) Treccani, L.; Yvonne Klein, T.; Meder, F.; Pardun, K.; Rezwan, K. Functionalized ceramics for biomedical, biotechnological and environmental applications. *Acta Biomater.* **2013**, *9*, 7115-7150.
(9) Jung, K. T.; Bell, A. T. The effects of synthesis and pretreatment conditions on the bulk structure and surface properties of zirconia. *J. Mol. Catal. A: Chem.* **2000**, *163*, 27-42.
(10) Tada, S.; Ochiai, N.; Kinoshita, H.; Yoshida, M.; Shimada, N.; Joutsuka, T.; Nishijima, M.; Honma, T.; Yamauchi, N.; Kobayashi, Y.; et al. Active Sites on $Zn_xZr_{1-x}O_{2-x}$ Solid Solution Catalysts for CO_2-to-Methanol Hydrogenation. *ACS Catal.* **2022**, *12*, 7748-7759.
(11) Perdew, J. P.; Burke, K.; Ernzerhof, M. Generalized Gradient Approximation Made Simple. *Phys. Rev. Lett.* **1996**, *77*, 3865-3868.
(12) Grimme, S.; Antony, J.; Ehrlich, S.; Krieg, H. A consistent and accurate ab initio parametrization of density functional dispersion correction (DFT-D) for the 94 elements H-Pu. *J. Chem. Phys.* **2010**, *132*, 154104.
(13) Kühne, T. D.; Iannuzzi, M.; Ben, M. D.; Rybkin, V. V.; Seewald, P.; Stein, F.; Laino, T.; Khaliullin, R. Z.; Schütt, O.; Schiffmann, F.; et al. CP2K: An electronic structure and molecular dynamics software package - Quickstep: Efficient and accurate electronic structure calculations. *J. Chem. Phys.* **2020**, *152*, 194103.
(14) Goedecker, S.; Teter, M.; Hutter, J. Separable dual-space Gaussian pseudopotentials. *Phys. Rev. B* **1996**, *54*, 1703-1710.
(15) Hartwigsen, C.; Goedecker, S.; Hutter, J. Relativistic separable dual-space Gaussian pseudopotentials from H to Rn. *Phys. Rev. B* **1998**, *58*, 3641-3662.
(16) VandeVondele, J.; Hutter, J. Gaussian basis sets for accurate calculations on molecular systems in gas and condensed phases. *J. Chem. Phys.* **2007**, *127*, 114105.
(17) Momma, K.; Izumi, F. VESTA 3 for three-dimensional visualization of crystal, volumetric and morphology data. *J. Appl. Crystallogr.* **2011**, *44*, 1272-1276.
(18) Mamott, G. T.; Barnes, P.; Tarling, S. E.; Jones, S. L.; Norman, C. J. Dynamic studies of zirconia crystallization. *J. Mater. Sci.* **1991**, *26*, 4054-4061.
(19) Turrillas, X.; Barnes, P.; Dent, A. J.; Jones, S. L.; Norman, C. J. 'Hydroxide' precursor to zirconia: extended X-ray absorption fine structure study. *J. Mater. Chem.* **1993**, *3*, 583-586, 10.1039/JM9930300583.
(20) Igawa, N.; Ishii, Y. Crystal Structure of Metastable Tetragonal Zirconia up to 1473 K. *J. Am. Ceram. Soc.* **2001**, *84*, 1169-1171.
(21) Nosé, S. A unified formulation of the constant temperature molecular dynamics methods. *J. Chem. Phys.* **1984**, *81*, 511-519.
(22) Hoover, W. G. Canonical dynamics: Equilibrium phase-space distributions. *Phys. Rev. A* **1985**, *31*, 1695-1697.
(23) Martyna, G. J.; Klein, M. L.; Tuckerman, M. Nosé–Hoover chains: The canonical ensemble via continuous dynamics. *J. Chem. Phys.* **1992**, *97*, 2635-2643.

(24) Martyna, G. J.; Tobias, D. J.; Klein, M. L. Constant pressure molecular dynamics algorithms. *J. Chem. Phys.* **1994**, *101*, 4177-4189.
(25) Zhao, X.; Ceresoli, D.; Vanderbilt, D. Structural, electronic, and dielectric properties of amorphous ZrO_2 from ab initio molecular dynamics. *Phys. Rev. B* **2005**, *71*, 085107.
(26) Rushton, M. J. D.; Ipatova, I.; Evitts, L. J.; Lee, W. E.; Middleburgh, S. C. Stoichiometry deviation in amorphous zirconium dioxide. *RSC Adv.* **2019**, *9*, 16320-16327, 10.1039/C9RA01865D.
(27) Wyckoff, R. W. G.; Wyckoff, R. W. *Crystal structures*; Interscience publishers New York, 1963.
(28) Sugiyama, K.; Waseda, Y.; Kudo, S. Structural Analysis of Hydrolytic Condensed Zirconium Oxide by the Anomalous X-ray Scattering Method. *ISIJ Int.* **1991**, *31*, 1362-1367.
(29) Soliz, J. R.; Klevitch, A. D.; Harris, C. R.; Rossin, J. A.; Ng, A.; Stroud, R. M.; Hauser, A. J.; Peterson, G. W. Structural Impact on Dielectric Properties of Zirconia. *J. Phys. Chem. C* **2016**, *120*, 26834-26840.
(30) Huang, C.; Tang, Z.; Zhang, Z. Differences between Zirconium Hydroxide ($Zr(OH)_4 \cdot nH_2O$) and Hydrous Zirconia ($ZrO_2 \cdot nH_2O$). *J. Am. Ceram. Soc.* **2001**, *84*, 1637-1638.
(31) Pokrovski, K.; Jung, K. T.; Bell, A. T. Investigation of CO and CO_2 Adsorption on Tetragonal and Monoclinic Zirconia. *Langmuir* **2001**, *17*, 4297-4303.
(32) Joutsuka, T. Molecular Mechanism of Autodissociation in Liquid Water: Ab Initio Molecular Dynamics Simulations. *J. Phys. Chem. B* **2022**.
(33) Piskorz, W.; Gryboś, J.; Zasada, F.; Zapała, P.; Cristol, S.; Paul, J.-F.; Sojka, Z. Periodic DFT Study of the Tetragonal ZrO_2 Nanocrystals: Equilibrium Morphology Modeling and Atomistic Surface Hydration Thermodynamics. *J. Phys. Chem. C* **2012**, *116*, 19307-19320.
(34) Piskorz, W.; Gryboś, J.; Zasada, F.; Cristol, S.; Paul, J.-F.; Adamski, A.; Sojka, Z. Periodic DFT and Atomistic Thermodynamic Modeling of the Surface Hydration Equilibria and Morphology of Monoclinic ZrO_2 Nanocrystals. *J. Phys. Chem. C* **2011**, *115*, 24274-24286.
(35) Zhao, K.; Wang, W.; Li, Z. Highly efficient Ni/ZrO_2 catalysts prepared via combustion method for CO_2 methanation. *J. CO2 Util.* **2016**, *16*, 236-244.
(36) CRC handbook of chemistry and physics. 80 ed.; Lide, D. R., Ed.; CRC Press: 1999.
(37) Peterson, G. W.; Rossin, J. A.; Karwacki, C. J.; Glover, T. G. Surface Chemistry and Morphology of Zirconia Polymorphs and the Influence on Sulfur Dioxide Removal. *J. Phys. Chem. C* **2011**, *115*, 9644-9650.
(38) Southon, P. D.; Bartlett, J. R.; Woolfrey, J. L.; Ben-Nissan, B. Formation and Characterization of an Aqueous Zirconium Hydroxide Colloid. *Chem. Mater.* **2002**, *14*, 4313-4319.
(39) Smith, D. K.; Newkirk, W. The crystal structure of baddeleyite (monoclinic ZrO_2) and its relation to the polymorphism of ZrO_2. *Acta Crystallogr.* **1965**, *18*, 983-991.
(40) McCullough, J. D.; Trueblood, K. N. The crystal structure of baddeleyite (monoclinic ZrO_2). *Acta Crystallogr.* **1959**, *12*, 507-511.
(41) Ricca, C.; Ringuedé, A.; Cassir, M.; Adamo, C.; Labat, F. A comprehensive DFT investigation of bulk and low-index surfaces of ZrO_2 polymorphs. *J. Comput. Chem.* **2015**, *36*, 9-21.
(42) Christensen, A.; Carter, E. A. First-principles study of the surfaces of zirconia. *Phys. Rev. B* **1998**, *58*, 8050-8064.
(43) Navrotsky, A. Energetics of nanoparticle oxides: interplay between surface energy and polymorphism†. *Geochem. Trans.* **2003**, *4*, 34.

(44) Zhang, Y. L.; Jin, X. J.; Rong, Y. H.; Hsu, T. Y.; Jiang, D. Y.; Shi, J. L. The size dependence of structural stability in nano-sized ZrO_2 particles. *Mater. Sci. Eng., A* **2006**, *438-440*, 399-402.
(45) Chagas, L. H.; Zonetti, P. C.; Matheus, C. R. V.; Rabello, C. R. K.; Alves, O. C.; Appel, L. G. The Role of the Oxygen Vacancies in the Synthesis of 1, 3-Butadiene from Ethanol. *ChemCatChem* **2019**, *11*, 5625-5632, 10.1002/cctc.201901243.
(46) Ticali, P.; Salusso, D.; Ahmad, R.; Ahoba-Sam, C.; Ramirez, A.; Shterk, G.; Lomachenko, K. A.; Borfecchia, E.; Morandi, S.; Cavallo, L.; et al. CO_2 hydrogenation to methanol and hydrocarbons over bifunctional Zn-doped ZrO_2/zeolite catalysts. *Catal. Sci. Technol.* **2021**, *11*, 1249-1268, 10.1039/D0CY01550D.
(47) Huang, J.; Wang, W.; Li, D.; Xu, S.; Liu, Q.; Chen, X.; Fei, Z.; Zhang, Z.; Cui, M.; Tang, J.; et al. Facile construction of non-crystalline ZrO_2 as an active yet durable catalyst for methane oxychlorination. *J. Sol-Gel Sci. Technol.* **2019**, *92*, 163-172.
(48) Haase, F.; Sauer, J. The Surface Structure of Sulfated Zirconia: Periodic ab Initio Study of Sulfuric Acid Adsorbed on ZrO_2(101) and ZrO_2(001). *J. Am. Chem. Soc.* **1998**, *120*, 13503-13512.
(49) Delarmelina, M.; Deshmukh, G.; Goguet, A.; Catlow, C. R. A.; Manyar, H. Role of Sulfation of Zirconia Catalysts in Vapor Phase Ketonization of Acetic Acid. *J. Phys. Chem. C* **2021**, *125*, 27578-27595.
(50) Keskitalo, T. J.; Veringa Niemelä, M. K.; Krause, A. O. I. Modeling of the Adsorption and Desorption of CO_2 on Cu/ZrO_2 and ZrO_2 Catalysts. *Langmuir* **2007**, *23*, 7612-7619.
(51) Ignatchenko, A. V. Density Functional Theory Study of Carboxylic Acids Adsorption and Enolization on Monoclinic Zirconia Surfaces. *J. Phys. Chem. C* **2011**, *115*, 16012-16018.
(52) Bazhenov, A. S.; Honkala, K. Understanding Structure and Stability of Monoclinic Zirconia Surfaces from First-Principles Calculations. *Top. Catal.* **2017**, *60*, 382-391.
(53) Mogilevsky, G.; Karwacki, C. J.; Peterson, G. W.; Wagner, G. W. Surface hydroxyl concentration on $Zr(OH)_4$ quantified by 1H MAS NMR. *Chem. Phys. Lett.* **2011**, *511*, 384-388.
(54) Redhead, P. A. Thermal desorption of gases. *Vacuum* **1962**, *12*, 203-211.
(55) Kouva, S.; Honkala, K.; Lefferts, L.; Kanervo, J. Review: monoclinic zirconia, its surface sites and their interaction with carbon monoxide. *Catal. Sci. Technol.* **2015**, *5*, 3473-3490, 10.1039/C5CY00330J.
(56) Gaspar, A. B.; Barbosa, F. G.; Letichevsky, S.; Appel, L. G. The one-pot ethyl acetate syntheses: The role of the support in the oxidative and the dehydrogenative routes. *Appl. Catal. A Gen.* **2010**, *380*, 113-117.
(57) Hirshfeld, F. L. Bonded-atom fragments for describing molecular charge densities. *Theor. Chim. Acta* **1977**, *44*, 129-138.
(58) Ciuparu, D.; Ensuque, A.; Shafeev, G.; Bozon-Verduraz, F. Synthesis and apparent bandgap of nanophase zirconia. *J. Mater. Sci. Lett.* **2000**, *19*, 931-933.
(59) Elmaslmane, A. R.; Watkins, M. B.; McKenna, K. P. First-Principles Modeling of Polaron Formation in TiO_2 Polymorphs. *J. Chem. Theory Comput.* **2018**, *14*, 3740-3751.
(60) Joutsuka, T.; Yoshinari, H.; Yamauchi, S. Facet Dependence of Photocatalytic Activity in Anatase TiO_2: Combined Experimental and DFT Study. *Bull. Chem. Soc. Jpn.* **2021**, *94*, 106-111.

TOC Graphic